Supporting Information: Fluctuating hydrogen-bond networks govern anomalous electron transfer kinetics in azurin

Kretchmer et al. 10.1073/pnas.1805719115

1. Potential Energy Surfaces

Expressed in the diabatic representation, the potential energy matrix for the Hamiltonian has the form

$$V(\mathbf{R}) = \begin{pmatrix} V_{\mathrm{A}}(\mathbf{R}) & H_{\mathrm{AB}}(\mathbf{R}) \\ H_{\mathrm{AB}}(\mathbf{R}) & V_{\mathrm{B}}(\mathbf{R}) \end{pmatrix}, \quad [1]$$

where the off-diagonal term, $H_{\mathrm{AB}}(\mathbf{R})$, is the electronic coupling defined in Eq. 6 in the main text, and $V_{\mathrm{A}}(\mathbf{R})$ and $V_{\mathrm{B}}(\mathbf{R})$ are the potential energy surfaces for the reactant and product electron transfer (ET) states, respectively. The vector of nuclear positions is given by $\mathbf{R}$.

The potential energy surfaces used to define the ET reactant and product states are based on the GROMOS 53a6 forcefield.(1) Two sets of partial charges were defined to characterize the bond polarization around the copper and ruthenium centers in the reactant and product states. Partial charges were determined following previous procedures with additional density functional theory calculations with point charge fitting using the CHELPG method.(2–4) The partial charges around the metal center are further scaled to capture the experimentally observed reorganization energy for WT, such that

$$Q_{\mathrm{A}} = \frac{1}{2}(q_{\mathrm{A}} + q_{\mathrm{B}}) + \frac{1}{2}\chi(q_{\mathrm{A}} - q_{\mathrm{B}}) \quad [2]$$

and

$$Q_{\mathrm{B}} = \frac{1}{2}(q_{\mathrm{A}} + q_{\mathrm{B}}) - \frac{1}{2}\chi(q_{\mathrm{A}} - q_{\mathrm{B}}), \quad [3]$$

where q_{A} and q_{B} are the original charges on the reactant and product state, respectively, Q_{A} and Q_{B} are the scaled charges, and the scaling factor is chosen to be $\chi = 0.68$. The scaled charges are left unchanged for the simulations of the mutants.

Harmonic bond and angle terms were added between the copper ion and the ligating atoms. The parameters in these terms were fit to preserve the deformed trigonal bipyramidal geometry observed in crystal structures. To capture fluctuations in atomic position at the ruthenium center, intermolecular interaction terms for the imidazole and bipyridine ligands were drawn from analogous bonds in the GROMOS 53a6 forcefield when available and from the generalized amber forcefield otherwise. In order to maintain the octahedral geometry, bond, angle, and torsional terms between the ruthenium and ligating atoms were added. Finally, weak torsional restraints were applied to all backbone atoms to prevent rare loop-flipping transitions and to focus sampling on configurations consistent with those observed in the crystal structure.

An additional constant term was added to the product state energy of the WT and each of three mutants to reproduce the experimentally determined driving forces for each reaction. The constant terms are −674 kJ/mol, −677 kJ/mol, −680 kJ/mol, and −682 kJ/mol for the WT, N47D, N47S, and N47L, respectively.

Example topology files for WT and the three mutants are provided as separate text documents, fully specifying all terms in the potential energy surface.

2. Calculation Details

The simulation box included the modified azurin protein and 4769 SPC/E water molecules. Initial coordinates for the protein and crystallographic waters were taken from chain A of the 1BEX protein data bank structure. Additional waters were added in an octahedral box with periodic boundary conditions. Relaxation on the reactant potential energy surface followed a series of NVT simulations with decreasingly strong positional restraints on all heavy crystallographic atoms and decreasingly strong distance restraints among the heavy atoms around residue 47 to maintain hydrogen bonds. Once all restraints were removed, a long NPT simulation of 50 ns was run to further relax the added solvating waters. Mutations to the N47 residue were made after these relaxation steps, and a series of NVT simulations were run for each mutant with decreasingly strong distance restraints among the heavy atoms around residue 47 to maintain possible hydrogen bonds.

After relaxation, all additional distance and positional restraints were removed, and all simulations were run at constant temperature and volume with temperature maintained by a velocity-scaling thermostat.(1) Reaction-field electrostatics were employed, and electrostatic and van der Waals interactions were cut off at 1.4 nm. A twin-range cut-off scheme was used with interactions greater than 0.8 nm updated every 10 steps.

3. KC-RPMD

The KC-RPMD equations of motion defined in Eq. 5 of the main text depend on the mass of the auxiliary electronic variable, m_y, the friction coefficient, γ_y, and derivatives of the KC-RPMD effective potential, $V_{\mathrm{eff}}(\mathbf{R}, y)$, where y is the auxiliary electronic variable and $\mathbf{R}$ is the position vector of all nuclear degrees of freedom.

The effective potential in the limit of classical nuclei is given by (5, 6)

$$V_{\mathrm{eff}}^{\mathrm{KC}}(\mathbf{R}, y) = -\frac{1}{\beta}\ln\left[\sum_{\{i^{(\alpha)}\}} g(\{i^{(\alpha)}\}, \mathbf{R}) e^{-\beta V_{\mathrm{r}}(y, \{i^{(\alpha)}\})} \prod_{\alpha=1}^{n} M_{i^{(\alpha)}, i^{(\alpha+1)}}(\mathbf{R})\right], \quad [4]$$

where $i^{(\alpha)}$ denotes the diabatic electronic state of the αth ring-polymer bead and in the SI, $\beta = (k_{\mathrm{B}}T)^{-1}$ is the inverse temperature. In the classical limit for the nuclei, the ring-polymer coordinates for the nuclear positions collapse to the classical positions of the atoms.

The penalty function that penalizes the formation of kink-pairs at nuclear configurations for which the diabatic surfaces are non-degenerate is given by

$$g(\{i^{(\alpha)}\},\mathbf{R})=\begin{cases} 1, & i^{(\alpha)}=0 \text{ for all } \alpha, \\ 1, & i^{(\alpha)}=1 \text{ for all } \alpha, \\ \left(\frac{a}{\pi}\right)^{\frac{1}{2}}\eta e^{-a(w(\mathbf{R}))^2}, & \text{otherwise}, \end{cases} \quad [5]$$

where the function $w(\mathbf{R}) = (V_{\mathrm{A}}(\mathbf{R}) - V_{\mathrm{B}}(\mathbf{R}))/H_{\mathrm{AB}}(\mathbf{R})$ is the scaled difference in the diabatic potential surfaces, a is a unitless convergence parameter, and the prefactor η is a multiplicative factor that is chosen to avoid biasing the probability of kink-pair formation at nuclear configurations for which the diabats cross, such that

$$\eta = 2\pi\frac{\langle H_{\mathrm{AB}}(\mathbf{R})\rangle_{\mathrm{c}}\left\langle|\mathbf{F}_{\mathrm{A}}(\mathbf{R})-\mathbf{F}_{\mathrm{B}}(\mathbf{R})|\,H_{\mathrm{AB}}(\mathbf{R})^2\right\rangle_{\mathrm{c}}}{\langle|\mathbf{F}_{\mathrm{A}}(\mathbf{R})-\mathbf{F}_{\mathrm{B}}(\mathbf{R})|\rangle_{\mathrm{c}}\langle H_{\mathrm{AB}}(\mathbf{R})^3\rangle_{\mathrm{c}}}. \quad [6]$$

Here, $\mathbf{F}_{\mathrm{A}}(\mathbf{R})$ and $\mathbf{F}_{\mathrm{B}}(\mathbf{R})$ are the force vectors associated with the reactant and product electronic states, respectively. The brackets denote an ensemble average constrained to the intersection of the diabatic surfaces, such that

$$\langle(\ldots)\rangle_{\mathrm{c}} = \frac{\int d\mathbf{R}\delta(V_A(\mathbf{R})-V_B(\mathbf{R}))(\ldots)e^{-\beta V_A(\mathbf{R})}}{\int d\mathbf{R}\delta(V_A(\mathbf{R})-V_B(\mathbf{R}))e^{-\beta V_A(\mathbf{R})}}. \quad [7]$$

The square-restraining potential, $V_{\mathrm{r}}(y,\{i^{(\alpha)}\})$, that tethers the auxiliary electronic variable to a discrete collective variable, $\theta(\{i^{(\alpha)}\})$, that reports on the existence of kink-pairs in the ring-polymer configuration, is defined such that

$$e^{-\beta V_{\mathrm{r}}(y,\{i^{(\alpha)}\})} = f(y,\theta(\{i^{(\alpha)}\})), \quad [8]$$

where

$$f(y,\theta) = \lim_{b\to\infty}\frac{1}{2l_\theta}\left(1-\tanh\left[b\left(|y-\theta|-\frac{l_\theta}{2}\right)\right]\right), \quad [9]$$

and

$$l_\theta = \begin{cases} L, & \theta(\{i^{(\alpha)}\})=0 \\ 2-L, & \text{otherwise.} \end{cases} \quad [10]$$

The discrete collective variable is given by

$$\theta(\{i^{(\alpha)}\}) = \begin{cases} -1, & i^{(\alpha)}=0 \text{ for all } \alpha, \\ 1, & i^{(\alpha)}=1 \text{ for all } \alpha, \\ 0, & \text{otherwise.} \end{cases} \quad [11]$$

The term $M_{i,i'}(\mathbf{R})$ denotes the i,i' element of the matrix

$$\mathbf{M}(\mathbf{R}) = \begin{pmatrix} e^{-\beta_n V_{\mathrm{A}}(\mathbf{R})} & -\beta_n H_{\mathrm{AB}}(\mathbf{R})e^{-\beta_n V_{\mathrm{A}}(\mathbf{R})} \\ -\beta_n H_{\mathrm{AB}}(\mathbf{R})e^{-\beta_n V_{\mathrm{B}}(\mathbf{R})} & e^{-\beta_n V_{\mathrm{B}}(\mathbf{R})} \end{pmatrix}, \quad [12]$$

where $\beta_n = \beta/n$ and n is the number of ring-polymer beads.

The mass of the auxiliary electronic variable is given by (5)

$$m_y = \frac{\hbar^2\beta^3}{2\pi L^2}\left[\frac{\langle H_{\mathrm{AB}}(\mathbf{R})\rangle_{\mathrm{c}}\left\langle|\mathbf{F}_A(\mathbf{R})-\mathbf{F}_B(\mathbf{R})|\,H_{\mathrm{AB}}(\mathbf{R})^2\right\rangle_{\mathrm{c}}}{\langle|\mathbf{F}_A(\mathbf{R})-\mathbf{F}_B(\mathbf{R})|\rangle_{\mathrm{c}}\langle H_{\mathrm{AB}}(\mathbf{R})^2\rangle_{\mathrm{c}}}\right]^2, \quad [13]$$

and the friction coefficient is given by (5)

$$\gamma_y = \frac{1}{2(2-L)}\sqrt{\frac{1-2\ln\left[\frac{2-L}{L}\left(\frac{a}{\pi}\right)^{1/2}\eta\beta^2\right]-4\langle\ln|H_{\mathrm{AB}}(\mathbf{R})|\rangle_c}{\beta m_y}}. \quad [14]$$

Table S1. KC-RPMD parameters

Parameter	WT	N47D	N47S	N47L
n	32			
a	1×10^{-13}			
b	400			
L	0.1			
η	3.67	1.93	1.80	3.73
$m_y/(\mathrm{amu}\times\mathrm{nm}^2)/10^{16}$	0.77	2.76	1.52	1.88
$\gamma_y/\mathrm{ps}^{-1}$	41.8	41.7	41.9	41.4

The calculated KC-RPMD parameters for WT and all three mutants are given in Table S1. The units for m_y follow from the fact that y and thus L are adimensional.(5) The small magnitude of m_y is due to the weak electronic coupling of the system.

4. Calculation of the ET Rate

In general, the KC-RPMD rate of a reaction can be calculated using (5, 6)

$$k^{\mathrm{KC-RPMD}} = k_{\mathrm{TST}}^{\mathrm{KC-RPMD}}\lim_{t\to\infty}\kappa(t), \quad [15]$$

where $k_{\mathrm{TST}}^{\mathrm{KC-RPMD}}$ is the transition-state theory (TST) estimate associated with the dividing surface $\xi(\mathbf{r})=\xi^\ddagger$, and has previously been defined.(5, 6) The position vector for the full system is given as $\mathbf{r}=\{\mathbf{R},y\}$. The transmission coefficient, $\kappa(t)$, corrects for dynamical recrossing at the dividing surface and is defined as

$$\kappa(t) = \frac{\langle\dot\xi_0 h\left(\xi(\mathbf{r}_t)-\xi^\ddagger\right)\rangle^\ddagger}{\langle\dot\xi_0 h(\dot\xi_0)\rangle^\ddagger}, \quad [16]$$

where $h(x)$ is the Heaviside function, and the subscripts 0 and t denote evaluation of the quantity from the trajectory at its initiation and after evolution for time t, respectively. Here, $\xi(\mathbf{r})$ is a collective variable that distinguishes between reactants and products, and the ensemble average

$$\langle\ldots\rangle^\ddagger = \frac{\int d\mathbf{r}\int d\mathbf{v}\; e^{-\beta H(\mathbf{r},\mathbf{v})}\delta(\xi(\mathbf{r})-\xi^\ddagger)(\ldots)}{\int d\mathbf{r}\int d\mathbf{v}\; e^{-\beta H(\mathbf{r},\mathbf{v})}\delta(\xi(\mathbf{r})-\xi^\ddagger)} \quad [17]$$

corresponds to the ensemble average constrained to the dividing surface.

As mentioned in the main text, we employ the "kink-pair" dividing surface, which corresponds to a choice of $\xi(\mathbf{r}) = y$, with $y^\ddagger = 0$. The transmission coefficients associated with this choice of dividing surface are shown in Fig. S1 for WT and all three mutants. The transmission coefficients are each calculated from 100 dynamical KC-RPMD trajectories initialized from configurations generated from long KC-RPMD trajectories constrained to the dividing surface. Due to the small values of m_y given in Table S1, we follow previous work and choose a larger value of $m_y = 0.01$ amu $\times$ nm^2 for the integration of the KC-RPMD equations of motion in the dynamical trajectories, which is still small in comparison to the mass of the nuclei, but allows for a reasonable time-step during integration.(5) To generate the dynamical trajectories we use a time step of $dt = 0.02$ fs and the friction coefficients given in Table S1.

The transmission coefficients in Fig. S1 are all observed to plateau rapidly to values greater than 0.92. This result indicates that the "kink-pair" dividing surface provides a proper description for the ET reaction in WT azurin and its mutants and that the ET rate can be accurately described by a TST rate employing this dividing surface. To avoid the full calculation of the KC-RPMD TST rate, $k_{\rm TST}^{\rm KC-RPMD}$, which can be done in principle, but involves the calculation of a multidimensional free energy profile,(5) we instead use a modified Marcus-type TST given by Eq. 4 in the main text, which properly accounts for the dynamical fluctuations of the protein by calculating the electronic coupling as an average over the dividing surface ensemble.

The reorganization energy present in Eq. 4 in the main text is calculated from KC-RPMD trajectories using (7–9)

$$\lambda_{\rm KC} = \frac{1}{2}\left(\langle \Delta V(\mathbf{R})\rangle_{y=1} - \langle \Delta V(\mathbf{R})\rangle_{y=-1}\right), \qquad [18]$$

where $\Delta V(\mathbf{R})$ is the energy difference between the reactant and product potential energy surfaces at a given nuclear configuration and $\langle \dots \rangle_{y=i}$ corresponds to the average in the distribution corresponding to $y = i$; a value of $y = 1$ corresponds to the product distribution.

5. Experimental Details

Salts for buffer preparations were obtained from J. T. Baker. Imidazole were from Sigma-Aldrich. Terrific broth was from BD Biosciences. All buffer and solutions were prepared using 18 MΩ-cm water, unless otherwise noted. Ru(2,2′-bipyridine)$_2$Cl$_2$ and [Ru(NH$_3$)$_6$]Cl$_3$ were from Strem Chemicals. Ru(NH$_3$)$_6$Cl$_3$ was recrystallized prior to use.(10) Ru(2,2′ bipyridine)$_2$CO$_3$ was prepared according to the literature.(11) UV-visible spectra were recorded on an Agilent 8453 diode array spectrophotometer. All data were collected ambient temperature (∼292 K).

Plasmids encoding for azurin mutants were generated using the Stratagene Quikchange protocol. Proteins were expressed and purified using established protocols.(12) Purity was assessed using UV-vis (ε = 5,600 M^{-1}cm^{-1} at 628 nm). Modification with [Ru(bpy)$_2$]$^{2+}$ was carried out according to the literature.(13) Purity of all Ru-His83-modified azurins was assayed using UV-visible spectroscopy(13) and mass spectrometry. Mass spectrometry was performed in the Caltech Protein/Peptide MicroAnalytical Laboratory (PPMAL) and typical mass spectra are shown below.

Electrochemistry was carried out using a standard three-electrode setup: homemade basal-plane graphite (www.graphitestore.com) working electrode;(14) Ag/AgCl reference electrode; Pt wire counter electrode. The working electrode was gently abraded with 600 grit wet/dry sandpaper and polished with 1 μM alumina power on a microcloth polishing pad for 30 seconds between each scan. For all voltammetry experiments, protein solutions were 300 μM in 50 mM sodium phosphate, 50 mM NaCl, pH 7.5. CVs were collected at a scan rate of 20 mV/s. DPVs were collected with the following parameters: pulse amplitude = 30 mv; pulse width = 100 ms; pulse period = 200 ms; sample width = 15 ms, increment = 2 mV. The potential of the observed waves was independent of concentration between 0.4 and 1 mM for each protein. Potentials were converted to NHE by adding 0.193 V.

Transient spectroscopic measurements were conducted in the Beckman Institute Laser Resource Center at Caltech. Excitation (500 nm) was provided by an optical parametric oscillator (Spectra-Physics, Quanta-Ray MOPO-700) pumped by the third-harmonic of a Q-switched Nd:YAG laser (Spectra-Physics, Quanta-Ray PRO-Series, 8 ns pulse width). For transient absorbance data collected at 490 nm, white probe light from a pulsed 75 W Xe arc lamp was used. For transient absorbance data collected at 632.8 nm, a HeNe laser was used. Other aspects of the instrumentation used to collected time-resolved data are described elsewhere.(15)

Kinetics traces were collected at 632.8 and 490 nm for each protein sample. In all cases, protein samples were reduced using 100-fold excess of sodium ascorbate and desalted using PD-10 columns into 50 mM sodium phosphate + 50 mM NaCl (pH 7.5). The samples were deoxygenated by repeated pump + argon backfill cycles and left under an argon atmosphere for data collection. Flash-quench experiments were carried out with 12 mM [Ru(NH$_3$)$_6$]Cl$_2$ added to the solutions. Data at 490 nm were fit using a biexponential function that takes into consideration signal from Ru excited-state decay, as well as absorbance changes corresponding to the ET reaction of interest. The first rate constant corresponds to decay of electronically excited Ru$^{\rm II}$ and the second corresponds to intramolecular electron transfer from Cu$^{\rm I}$ to Ru$^{\rm III}$.

1. Oostenbrink C, Villa A, Mark A, van Gunsteren W (2004) A biomolecular force field based on the free enthalpy of hydration and solvation: the gromos force-field parameter sets 53a5 and 53a6. *J. Comput. Chem.* 13:1656–1676.
2. van den Bosch M, et al. (2005) Calculation of the redox potential of the protein azurin and some mutants. *Chembiochem* 4:738–746.
3. Ungar LW, Newton MD, Voth GA (1999) Classical and quantum simulation of electron transfer through a polypeptide. *J. Phys. Chem. B* 103:7367–7382.
4. Breneman C, Wiberg K (1990) Determining atom-centered monopoles from molecular electrostatic potentials - the need for high sampling density in formamide conformational-analysis. *J. Comput. Chem.* 11:361–373.
5. Kretchmer JS, Miller, III TF (2016) Kinetically-constrained ring-polymer molecular dynamics for non-adiabatic chemistries involving solvent and donor-acceptor dynamical effects. *Faraday Discuss.* 195:191.
6. Menzeleev AR, Bell F, Miller, III TF (2014) Kinetically constrained ring-polymer molecular dynamics for non-adiabatic chemical reactions. *J. Chem. Phys.* 140:064103.
7. Warshel A (1982) Dynamics of reactions in polar solvents. semiclassical trajectory studies of electron-transfer and proton-transfer reactions. *J. Phys. Chem.* 86:2218.
8. King G, Warshel A (1990) Investigation of the free energy functions for electron transfer reactions. *J. Chem. Phys.* 93:8682.
9. Small DW, Matyushov DV, Voth GA (2003) The theory of electron transfer reactions: What may be missing? *J. Am. Chem. Soc.* 125:7470.
10. Meyer T, Taube H (1968) Electron-transfer reactions of ruthenium ammines. *Inorg. Chem.* 7(11):2369–&.
11. Johnson EC, Sullivan BP, Salmon DJ, Adeyemi SA, Meyer TJ (1978) Synthesis and properties of chloro-bridged dimer [(bpy)2RuCl]22+ and its transient 3+ mixed-valence ion. *Inorg. Chem.* 17(8):2211–2215.
12. Chang T, et al. (1991) Gene synthesis, expression, and mutagenesis of the blue copper proteins azurin and plastocyanin. *Proc. Natl. Acad. Sci.* 88(4):1325–1329.
13. Faham S, et al. (1999) Structures of ruthenium-modified Pseudomonas aeruginosa azurin and [Ru(2,2 '-bipyridine)(2)(imidazole)(2)]SO4 center dot 10H(2)O. *Acta Crystallogr D Biol Crystallogr* 55(2):379–385.
14. Hanson SS, Warren JJ (2017) Syntheses, characterization, and electrochemical behavior of alkylated 2-(2′-quinolylbenzimidazole) complexes of rhenium (i). *Canadian Journal of Chemistry* 96(2):119–123.
15. Dempsey JL, Winkler JR, Gray HB (2010) Kinetics of Electron Transfer Reactions of H-2-Evolving Cobalt Diglyoxime Catalysts. *J. Am. Chem. Soc.* 132(3):1060–1065.

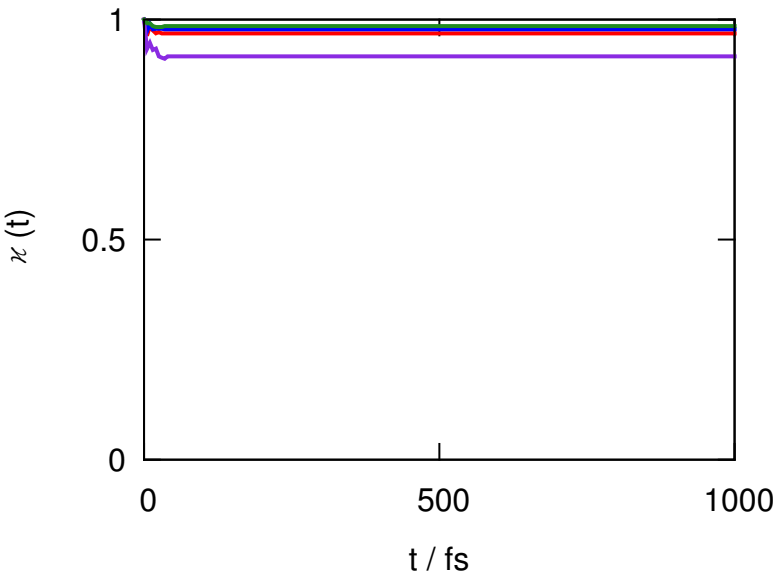

Fig. S1. The time-dependent transmission coefficient, $\kappa(t)$ (Eq. (16)), for WT (red), N47D (purple), N47S (green), and N47L (blue). The transmission coefficients all plateau rapidly to values greater than 0.92.

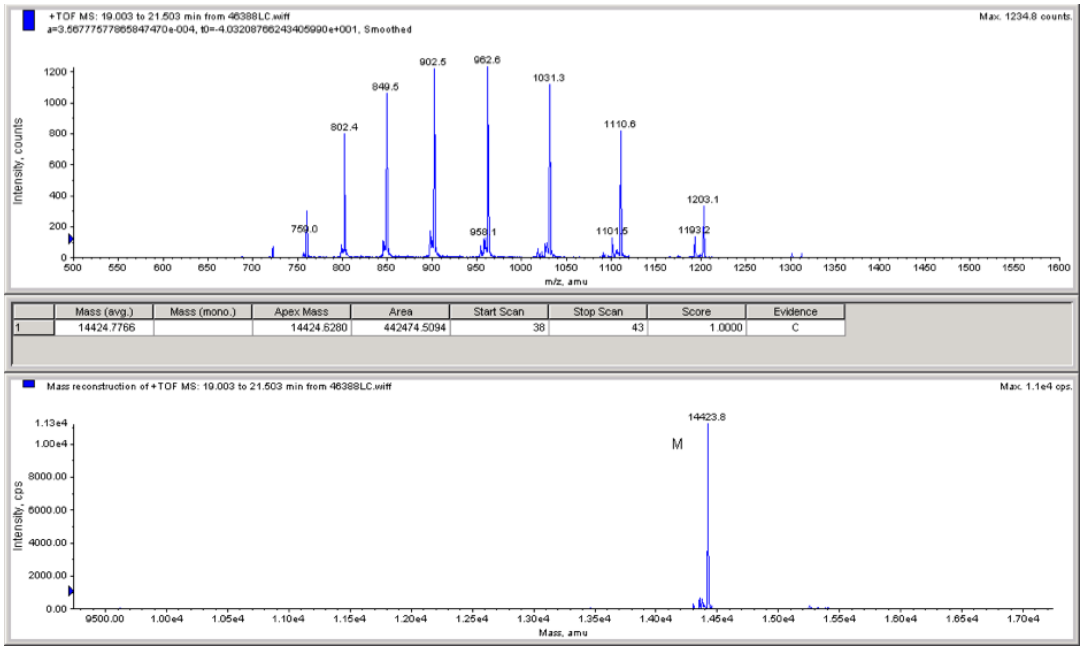

Fig. S2. Mass spectrum of N47-RuH83 azurin. Calculated = 14427.3, observed = 14424.7.

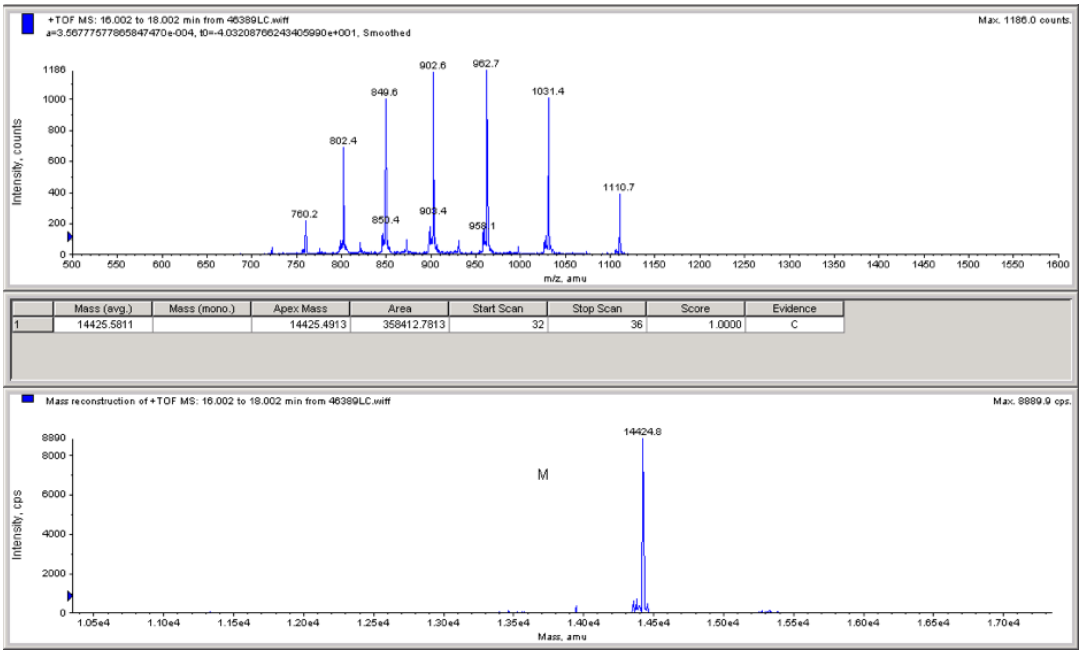

	Mass (avg.)	Mass (mono.)	Apex Mass	Area	Start Scan	Stop Scan	Score	Evidence
1	14425.5811		14425.4913	358412.7813	32	36	1.0000	C

Fig. S3. Mass spectrum of D47-RuH83 azurin. Calculated = 14428.3, observed = 14425.6

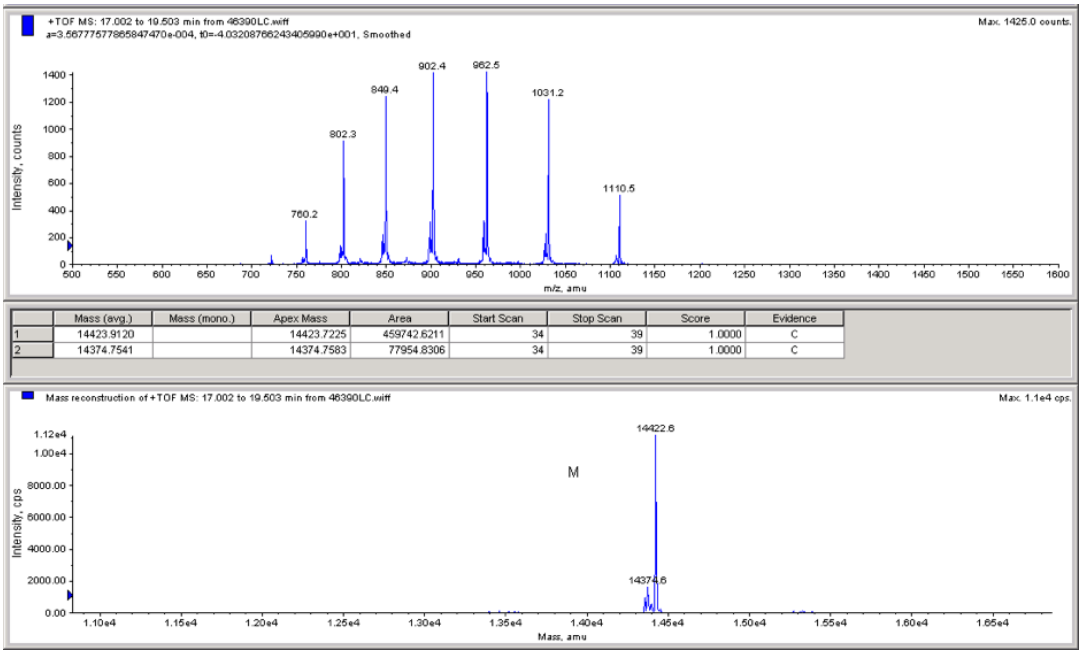

	Mass (avg.)	Mass (mono.)	Apex Mass	Area	Start Scan	Stop Scan	Score	Evidence
1	14423.9120		14423.7225	459742.6211	34	39	1.0000	C
2	14374.7541		14374.7583	77954.8306	34	39	1.0000	C

Fig. S4. Mass spectrum of L47-RuH83 azurin. Calculated = 14426.4, observed = 14423.9

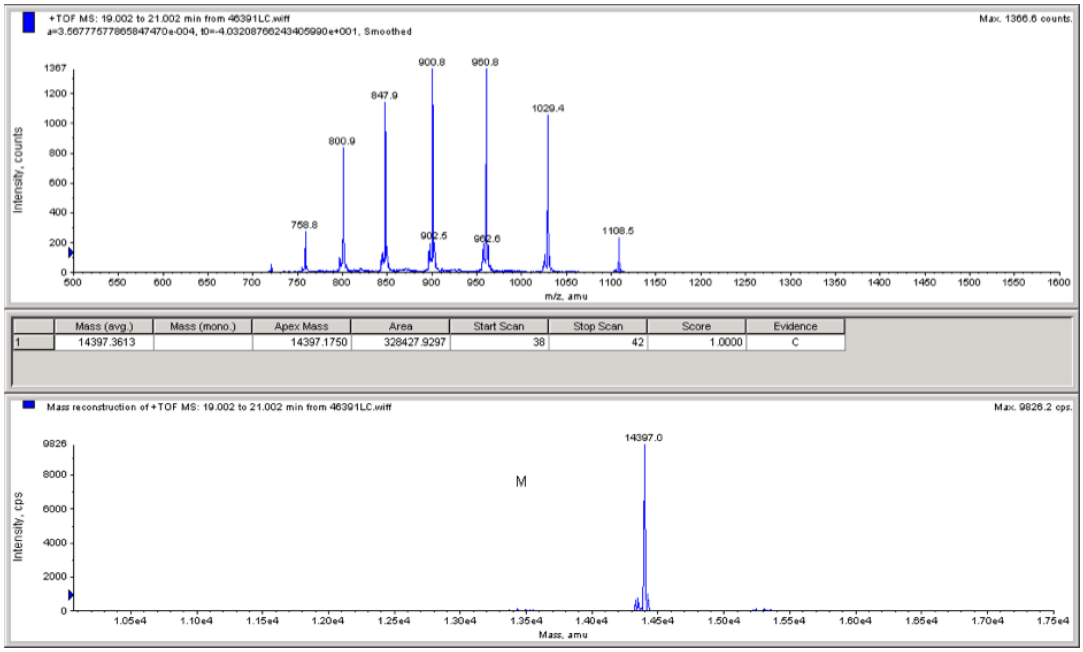

Fig. S5. Mass spectrum of S47-RuH83 azurin. Calculated = 14400.3, observed = 14397.4

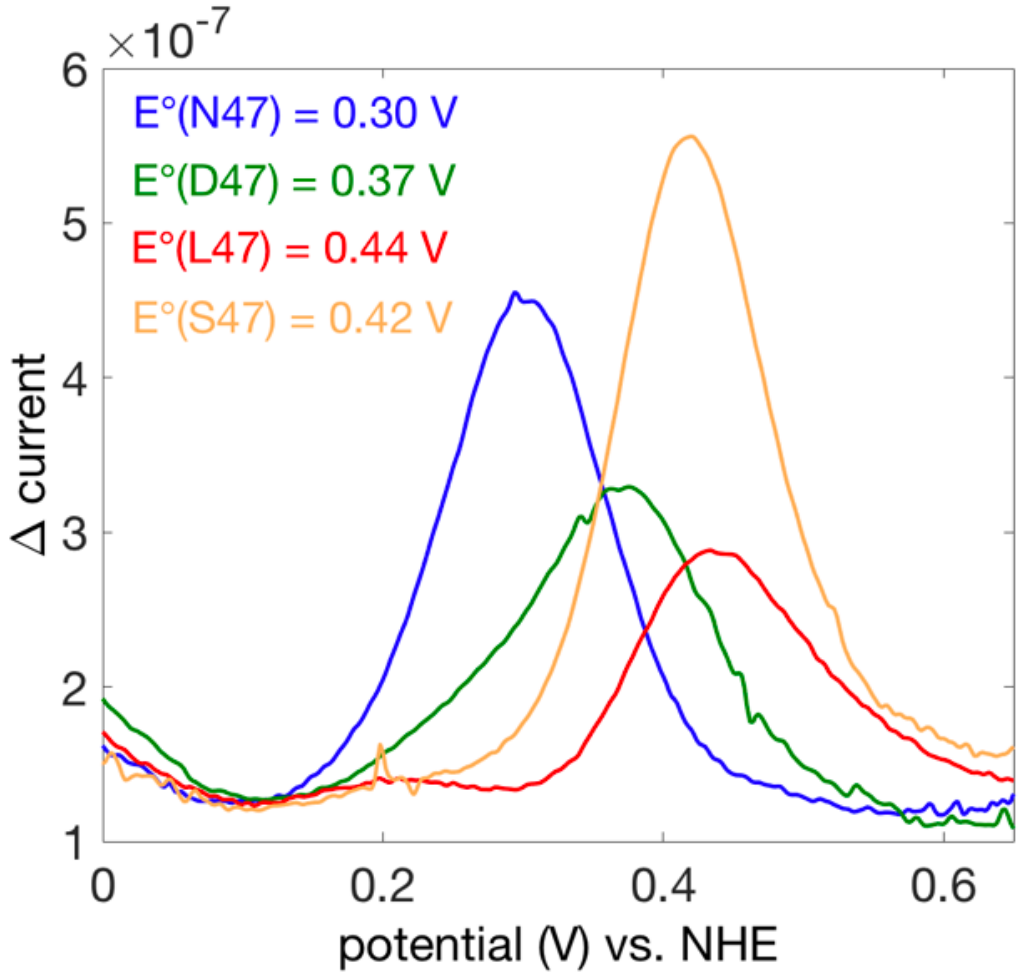

Fig. S6. Differential pulse voltammograms of X47 azurins (300 μM in 50 mM sodium phosphate, 50 mM NaCl, pH 7.5). Error associated with each potential is $\pm$ 0.02 V.

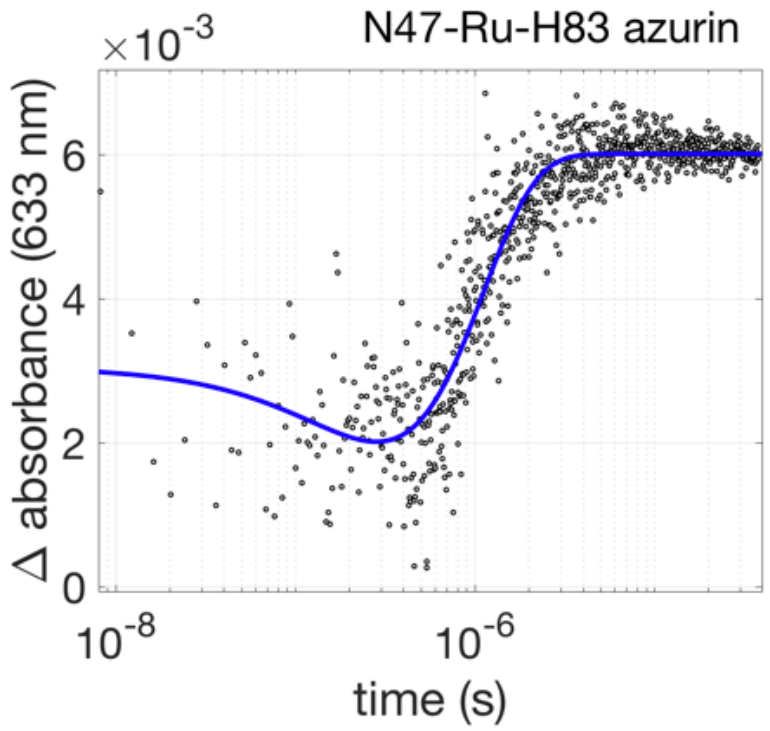

Fig. S7. Single wavelength kinetics trace at 633 nm for electron transfer from Cu^{I} to Ru^{III} in N47-Ru-H83 azurin (open circles) and biexponential fit (blue line). The absorbance for the initial (fast) phase corresponds to production and quenching (by $[Ru(NH_3)_6]^{2+}$) of electronically excited Ru^{II} (*Ru). The second, slower kinetics phase, corresponds to electron transfer from flash-quench generated Ru^{III} to azurin-Cu^{I} to make Cu^{II} (λ_{max} = 628 nm). The rate constant, k, for this process is $(1.0 \pm 0.1)\times 10^{6}$ s^{-1}.

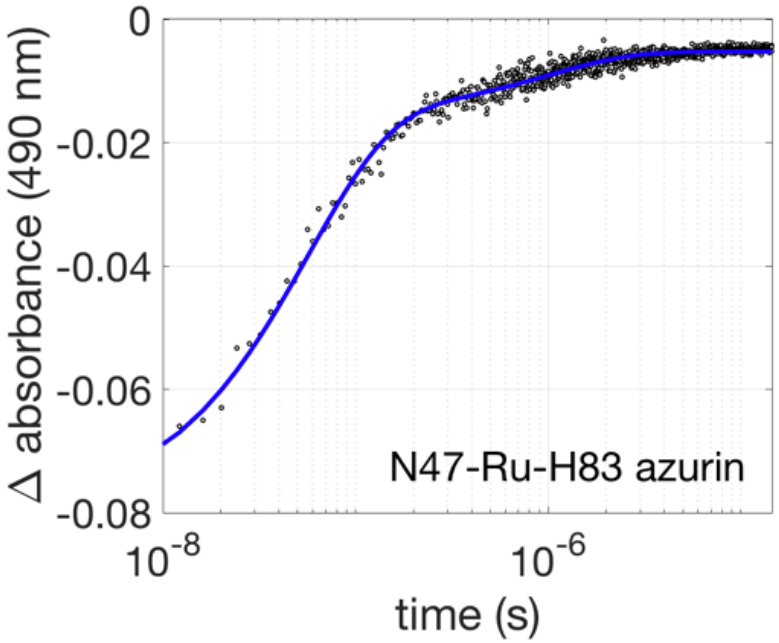

Fig. S8. Single wavelength kinetics trace at 490 nm for electron transfer from Cu^{I} to Ru^{III} in N47-Ru-H83 azurin (open circles) and biexponential fit (blue line). The initial (fast) phase corresponds to a bleach in the absorbance band of the Ru^{II} label due to the production of electronically excited Ru^{II} (*Ru) and subsequent quenching by $[Ru(NH_3)_6]^{2+}$. The second, slower kinetics phase, corresponds to electron transfer from flash-quench generated Ru^{III} to azurin-Cu^{I}. The rate constant, k, for this process is $(1.0 \pm 0.1)\times 10^{6}$ s^{-1}.

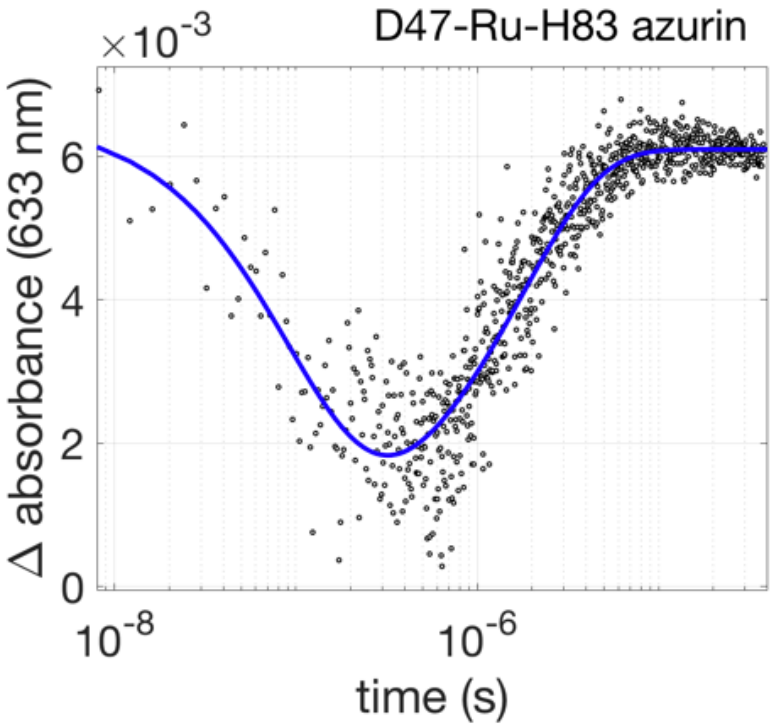

Fig. S9. Single wavelength kinetics trace at 633 nm for electron transfer from Cu^{I} to Ru^{III} in D47-Ru-H83 azurin (open circles) and biexponential fit (blue line). The absorbance for the initial (fast) phase corresponds to production and quenching (by $[Ru(NH_3)_6]^{2+}$) of electronically excited Ru^{II} (*Ru). The second, slower kinetics phase, corresponds to electron transfer from flash-quench generated Ru^{III} to azurin-Cu^{I} to make Cu^{II} (λ_{max} = 628 nm). The rate constant, k, for this process is (5.5±0.4)×10^5 s^{-1}.

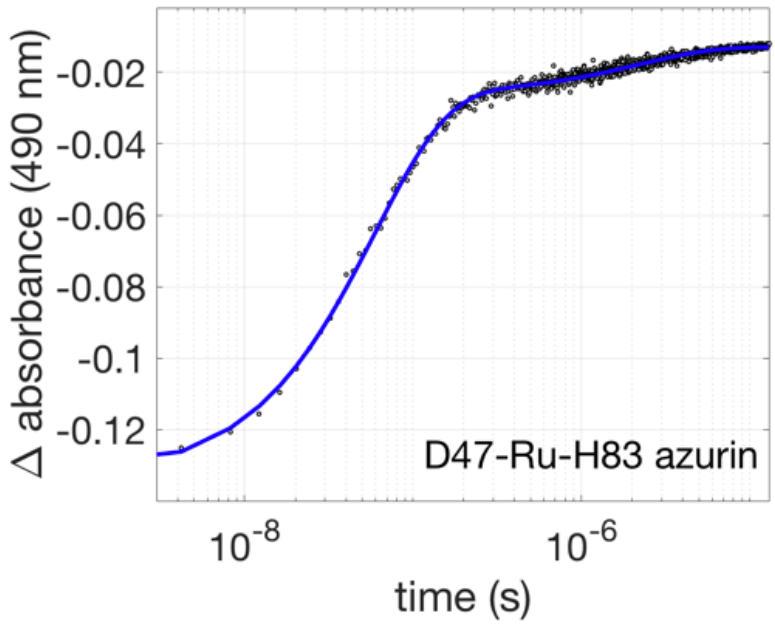

Fig. S10. Single wavelength kinetics trace at 490 nm for electron transfer from Cu^{I} to Ru^{III} in D47-Ru-H83 azurin (open circles) and biexponential fit (blue line). The initial (fast) phase corresponds to a bleach in the absorbance band of the Ru^{II} label due to the production of electronically excited Ru^{II} (*Ru) and subsequent quenching by $[Ru(NH_3)_6]^{2+}$. The second, slower kinetics phase, corresponds to electron transfer from flash-quench generated Ru^{III} to azurin-Cu^{I}. The rate constant, k, for this process is (4.5±0.1)×10^6 s^{-1}.

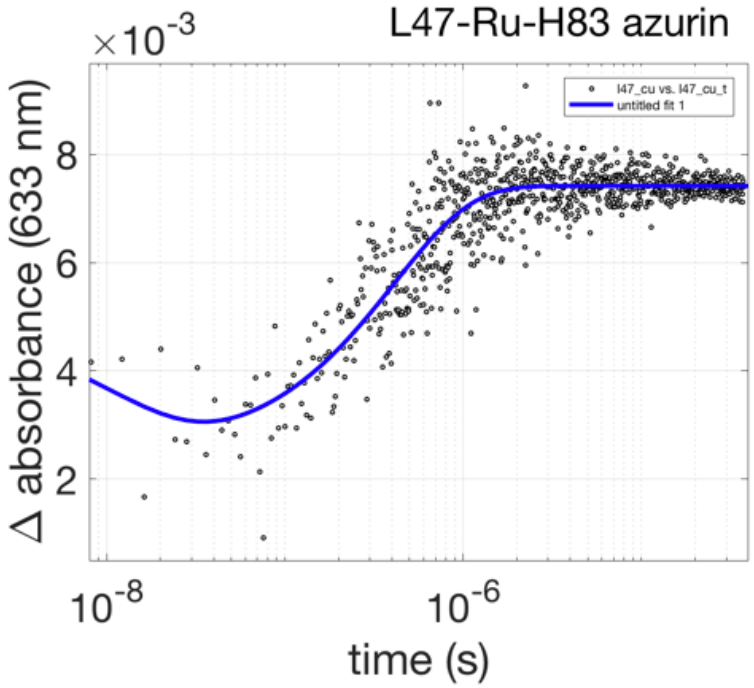

Fig. S11. Single wavelength kinetics trace at 633 nm for electron transfer from Cu^{I} to Ru^{III} in L47-Ru-H83 azurin (open circles) and biexponential fit (blue line). The absorbance for the initial (fast) phase corresponds to production and quenching (by $[Ru(NH_3)_6]^{2+}$) of electronically excited Ru^{II} (*Ru). The second, slower kinetics phase, corresponds to electron transfer from flash-quench generated Ru^{III} to azurin-Cu^{I} to make Cu^{II} (λ_{max} = 628 nm). The rate constant, k, for this process is (2.4±0.2)$\times 10^6$ s^{-1}.

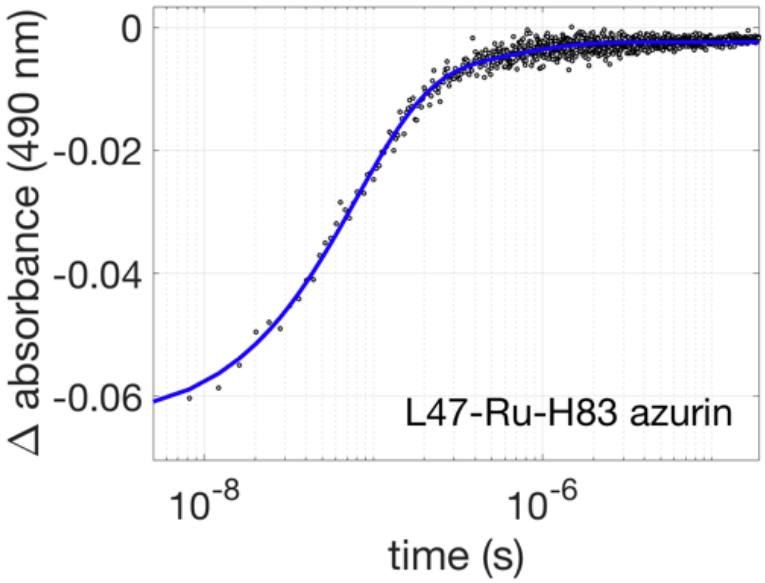

Fig. S12. Single wavelength kinetics trace at 490 nm for electron transfer from Cu^{I} to Ru^{III} in L47-Ru-H83 azurin (open circles) and biexponential fit (blue line). The initial (fast) phase corresponds to a bleach in the absorbance band of the Ru^{II} label due to the production of electronically excited Ru^{II} (*Ru) and subsequent quenching by $[Ru(NH_3)_6]^{2+}$. The second, slower kinetics phase, corresponds to electron transfer from flash-quench generated Ru^{III} to azurin-Cu^{I}. The rate constant, k, for this process is (1.7±0.2)$\times 10^6$ s^{-1}.

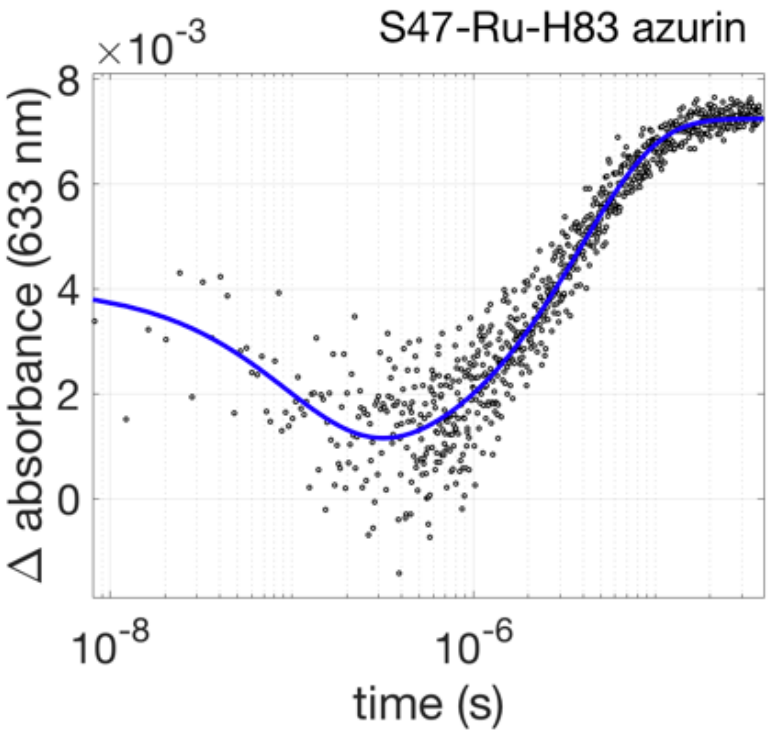

Fig. S13. Single wavelength kinetics trace at 633 nm for electron transfer from Cu^{I} to Ru^{III} in S47-Ru-H83 azurin (open circles) and biexponential fit (blue line). The absorbance for the initial (fast) phase corresponds to production and quenching (by $[Ru(NH_3)_6]^{2+}$) of electronically excited Ru^{II} (*Ru). The second, slower kinetics phase, corresponds to electron transfer from flash-quench generated Ru^{III} to azurin-Cu^{I} to make Cu^{II} (λ_{max} = 628 nm). The rate constant, k, for this process is (2.6±0.2)×10^5 s^{-1}.

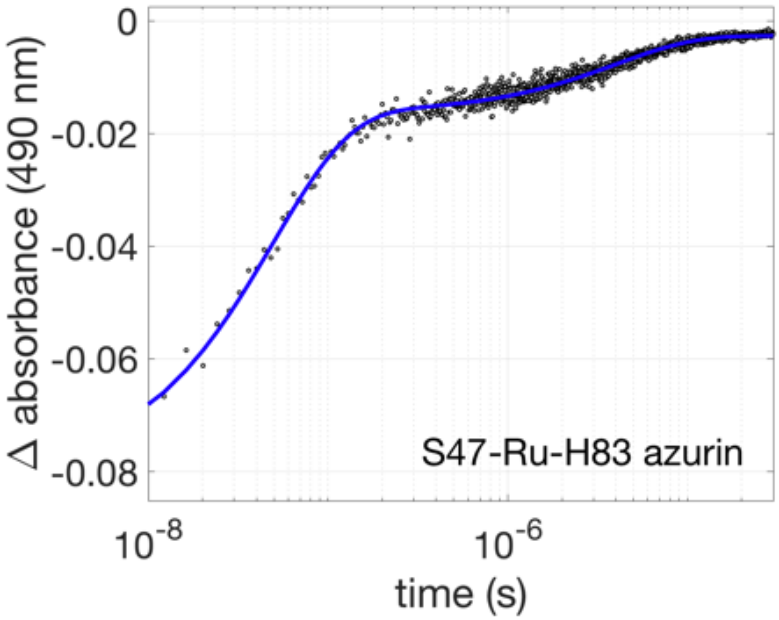

Fig. S14. Single wavelength kinetics trace at 490 nm for electron transfer from Cu^{I} to Ru^{III} in S47-Ru-H83 azurin (open-circles) and biexponential fit (blue line). The initial (fast) phase corresponds to a bleach in the absorbance band of the Ru^{II} label due to the production of electronically excited Ru^{II} (*Ru) and subsequent quenching by $[Ru(NH_3)_6]^{2+}$. The second, slower kinetics phase, corresponds to electron transfer from flash-quench generated Ru^{III} to azurin-Cu^{I}. The rate constant, k, for this process is (2.5±0.1)×10^5 s^{-1}.

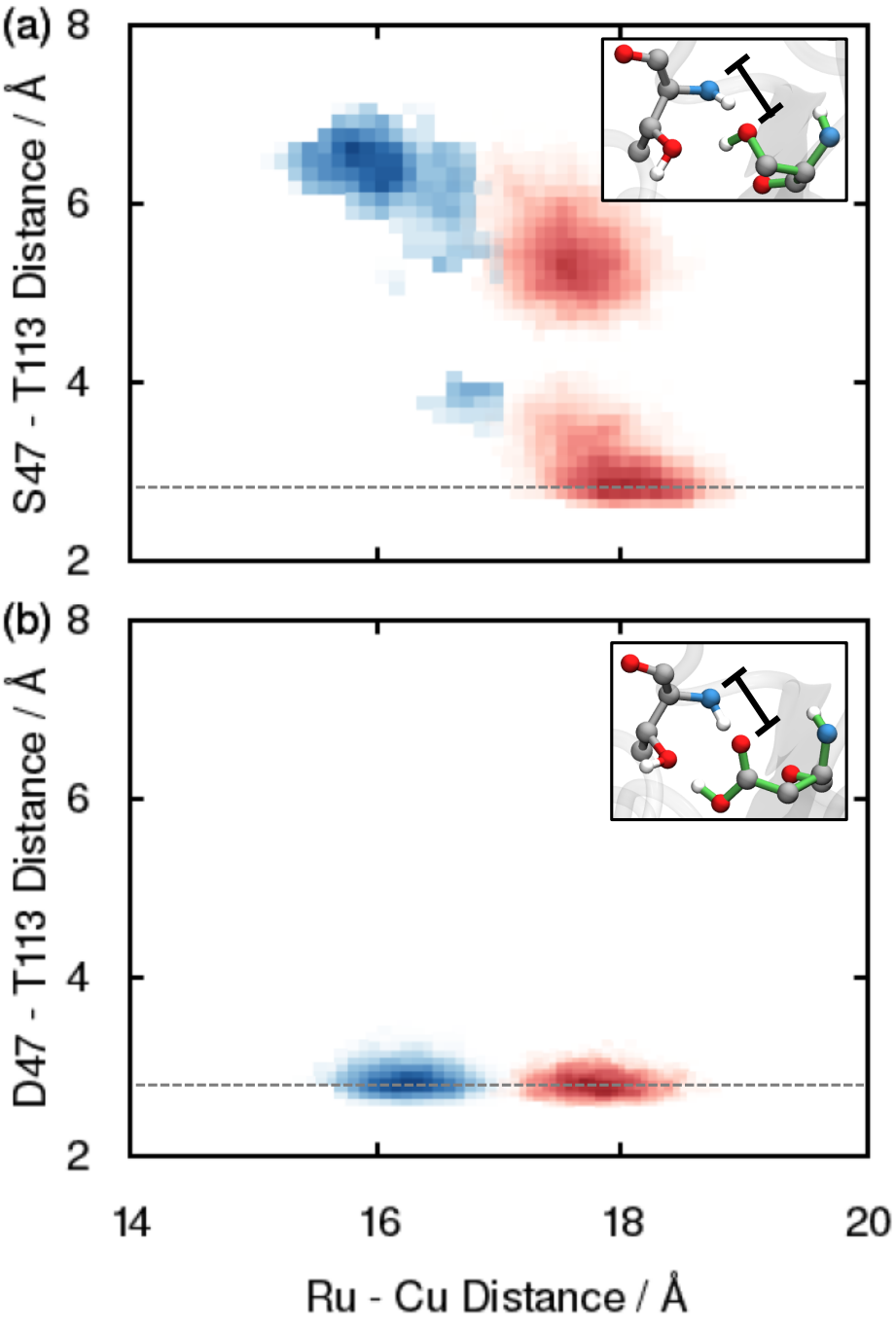

Fig. S15. Two-dimensional histogram of the Ru - Cu distance and the hydrogen-bonding distance between residue 47 and the nearby T113 for (a) N47S and (b) N47D. Reactant basin and dividing surface configurations are indicated by red and blue, respectively. The dashed lines indicate the average hydrogen-bond distance for the WT in the reactant basin. The insets indicate characteristic configurations for the two cases, with the hydrogen bond distance indicated. The hydrogen bond distance is defined as the distance between the backbone nitrogen on T113 and the hydroxyl oxygen on S47 for N47S and as the distance between the backbone nitrogen on T113 and the carbonyl oxygen on D47 for N47D. For the N47S mutant, the majority of the reactant population corresponds to a formed hydrogen bond (the darker red population) and the dividing surface ensemble exhibits a fully broken hydrogen bond, similar to WT behavior.